

Author version :Ocean Dynamics, vol.68(1); 2018; 1-16)

Hindcast of breaking waves and its impact at an island sheltered coast, Karwar

G. Udhaba Dora*, V. Sanil Kumar

*Corresponding author: Scientist, CSIR-National Institute of Oceanography (Council of Scientific and Industrial Research), Regional Centre, Lokhandawala Road, Andheri (West), Mumbai 400 053 India.

Email: udhaba@nio.org, Tel: +912226359605 Extn 2017, URL: www.nio.org

Senior Principal Scientist, Ocean Engineering, CSIR-National Institute of Oceanography (Council of Scientific and Industrial Research), Dona Paula, Goa 403 004 India.

Email: sanil@nio.org, Tel: +918322450327, URL: www.nio.org

Abstract

Variability in the characteristics of depth-induced wave breakers along a non-uniform coastal topography and its impact on the morpho-sedimentary processes is examined at the island sheltered wave-dominated micro-tidal coast, Karwar, west coast of India. Waves are simulated using the coupled wind wave model, SWAN nested in WAVEWATCH III, forced by the reanalysis winds from different sources (NCEP/NCAR, ECMWF, and NCEP/CFSR). Impact of the wave breakers is evaluated through mean longshore current and sediment transport for various wave energy conditions across different coastal morphology. Study revealed that the NCEP/CFSR wind is comparatively reasonable in simulation of nearshore waves using the SWAN model nested by 2D wave spectra generated from WAVEWATCH III. The Galvin formula for estimating mean longshore current using the crest wave period and the Kamphuis approximation for longshore sediment transport is observed realistic at the sheltered coastal environment while the coast interacts with spilling and plunging breakers.

Keywords: Surface gravity wave, longshore current, sediment transport, coastal processes, Eastern Arabian Sea

1- Introduction

Coastal zones are one of the major sources for development of a nation's economy. In consideration of the importance of coastal environment, the integrated coastal zone management (ICZM) has been widely implemented for collection of scientific information to understand coastal dynamics. Concerning the physical aspect, earlier observation shows that the depth-induced breaker plays a major role in sediment transport and successively it impacts on beach and shoreline stability (CEM 2006). Breaking wave is the terminal form of surface gravity wave that transports the wave energy to coastal morphology. The major characteristics of breaking waves: wave energy (height), angle of wave approach to coast (direction), and number of wave occurrence (period), are responsible for longshore morpho-sedimentary processes, while the magnitude of sediment transport generated by breaking waves is also controlled by the composition of associated sedimentary environment (CERC 1984; Kamphuis 2013). Also, breaking wave controls the rip current flow regimes and surfzone retention (Pitman et al. 2016). The characteristics of surface gravity wave travelling from open ocean transform due to refraction, diffraction and shoaling, and these waves superimpose locally generated wind waves (Chen et al. 2005; Londhe and Deo 2004). Further, the existence of land and sea breezes with diurnal scale is a typical phenomenon in coastal areas (Schmidt 1947). Thus, the intensity of breaking waves is directly related to swells, local wind pattern, and coastal morphology. Hence, non-uniformity in the behaviour of breaking wave, associated sediment transport, beach erosion/accretion processes, as well as shoreline advance and retreat, is natural. Along the shore, variability in the characteristics of breaking waves can be easily observed at an island sheltered coastal environment due to its complex bathymetry. Thus, simulation of spatio-temporal breaking waves using a wind-wave model is highly useful apart from field observations since in situ measurements that use multiple instruments are expensive, and gathering of long-term observations takes time. As the sea surface wind is the main source for generation of surface gravity waves, finding an appropriate wind source for wave simulation is essential to the wind-wave model. These backgrounds reveal the importance of numerical model for understanding the different conditions of breaking wave in space and time, and its impact on morpho-sedimentary processes.

The depth-induced breaking waves have been classified into four different types (spilling, plunging, collapsing, or surging) based on the physical changes of the surface profile during the breaking process (Galvin 1972). The depth-induced breakers have been estimated following the breaker index (γ) and the proportional coefficient of the rate of dissipation (α). The breaker index is the ratio of the maximum wave height (H_{\max}) to the respective water depth (d), i.e. $\gamma = H_{\max}/d$ (Battjes and Janssen (1978)), and the rate of dissipation is the ratio of orbital velocity to

phase velocity. The concept of the proportional coefficient of the rate of dissipation was demonstrated by Iverson (1952), who observed that the crest particle velocity is equal to the phase velocity at the point of breaking. Earlier, Kaminsky and Kraus (1993) reported a range of the breaker index from 0.6 to 1.59 with an average of 0.79, and thereby, Nelson (1997) observed the lowest breaker index was 0.55. However, Kaminsky and Kraus (1993) reported that no specific unique condition can be considered for estimation of breaking wave as it varies across different coastal morphology. However, the experiment on α was very less which has been considered as 1 in numerical prediction. Babanin (2011) reported that the alpha is at most 0.81 in the plunging breakers and 0.95 in the spilling breaker. Thereafter, Tissier et al. (2012) explained the breaking criteria based on wave front slope and critical slope. Followed by these observations, a study was considered to analyze the diversity in the formation of depth-induced breakers and its impact on different energy environment along the sandy beaches at the island sheltered wave-dominated micro-tidal coast, Karwar (Figure 1).

Karwar is a port town located on the Karnataka coast, part of the West Coast of India (WCI). The WCI is strongly dominated by seasonal climates, where the summer monsoon (hereafter monsoon) period varies from June to September, and the remaining eight months (non-monsoon) are under a fair weather condition. During monsoon, the wave climate is very rough, whereas that is calm to moderate during remaining period. The sandy beaches are highly dynamic during the monsoon due to high intensity waves, whereas the beaches are less dynamic during the non-monsoon period as the coast interacts with weak breakers. Along the Karnataka coast, Kumaret al. (2006) reported that about 75% of the total shoreline is covered by sandy beaches, and the variation of breaking waves follows a strong seasonal pattern along the open coast (Shanas and Kumar 2014). However, the formation of breaking waves and its impact in the sheltered coastal zone along the WCI are not well understood across the successive monsoons, and hence this area was selected to fulfill the considered objectives.

2. Methodology

2.1. Study location

The offshore/nearshore islands in this domain are (1) Kurmagadgudda, (2) Shimisgudda (Sungniri), (3) Devgadgudda, (4) Mandalgudda, (5) Karkaigudda, and (6) East Island, as reported in Chart No. 2008 of the Naval (National) Hydrographic Office (Figure 1). The Kali River originates from the Western Ghats and drains into the Arabian Sea at the Karwar coast, and it has a width of around 800 m at the river mouth. The beaches lie in a wave dominated micro-tidal estuarine coastal environment,

and the coast is dominated by southwest (SW) high energy waves (Dora and Kumar 2015). Further, the beaches were found uncertainly stable during annual cycles followed by non-uniform intra-annual sediment accretion/erosion (Nayak 1993; Hanamgond and Mitra 2007; Vinayaraj et al. 2011; Dora et al. 2012, 2014). Earlier observation revealed that the wind in this domain exhibits both the land and sea breezes in diurnal scale, where the nearshore waves follow a strong seasonal pattern during an annual cycle (Dora and Kumar 2015). During 2008-2010, the sea surface was considerably composed by wind-seas (36%) and swells (64%), while the peak wave direction (D_p) were from 186 to 323° with a range of peak wave period (T_p) from 3 to 22 s. The annual average significant wave height (H_{sig}) at 7 m water depth (NWB) was 0.8 m with a peak H_{sig} of 3.6 m and that was during the monsoon period (Dora and Kumar 2015).

In this study, the spatio-temporal variation of depth-induced breakers and its impact on beach morpho-sedimentary environment was analyzed at the six locations from BM1 to BM6 along the Karwar shoreline (Figure 1). Three locations (BM1, BM2, and BM3) were selected along the Devbag beach situated north of the Kali River mouth, and other three locations (BM4, BM5, and BM6) were along the Ravindranath Tagore (RT) beach situated at south. The selected six locations were enclosed by individual coastal topography. Earlier, Dora and Kumar (2015) studied the nearshore wave propagation along the shore, and observed different wave energy along the six locations. The BM1 location was partially sheltered from high energy SW waves, and the BM2 location was fully sheltered during the complete annual cycle by nearshore islands (Kurmagadgudda and Shimisgudda). The BM3 and BM4 locations were near to the Kali River mouth, and they were also open to SW waves. In an annual cycle, the BM5 location was exposed to the nearshore waves while the BM6 location was sheltered by the Karwar headland during most of the time. Further, the nearshore zone was observed as being partially protected by four offshore islands (Devgadgudda, Mandalgudda, Karkaigudda, and East Island) where the protection zone varies seasonally depending on the wave propagation to the coast.

2.2. Model setup and input parameter

One of the well-established wind-wave model, SWAN (Simulating WAVes Nearshore) nested in WWIII (WAVEWATCH III) (Booij et al. 1999; Tolman 2014) was executed to estimate the depth-induced breakers. The wind input for WWIII was collected from different sources: the National Centers for Environmental Prediction and the National Center for Atmospheric Research

(NCEP/NCAR) wind (Kalnay et al. 1996), the European Centre for Medium-Range Weather Forecasts (ECMWF) wind (Dee 2011), and the National Centers for Environmental Prediction and Climate Forecast System Reanalysis (NCEP/CFSR) wind (Saha 2010). Spatial resolution of NCEP/NCAR, ECMWF and NCEP/CFSR winds are $2.50^{\circ} \times 2.50^{\circ}$, $0.75^{\circ} \times 0.75^{\circ}$, and $0.50^{\circ} \times 0.50^{\circ}$ respectively, while temporal resolution are 6, 6, and 1 h. The NCEP/NCAR wind data at 0.995 sigma level represents 42 m above the ground (Faucher 1999), whereas the NCEP/CFSR and ECMWF wind data are at 10 m. The NCEP/NCAR wind data was converted to 10 m elevation (U_{10}) with respect to MSL based on the wind profile power law (Roland 1988) as per Eq. (1).

$$U_{10} = U_R * [10/R]^P \quad (1)$$

where, U_R is the wind speed that is measured at a fixed elevation (R) and used as reference wind speed, and P is the power law exponent and is equal to 1/7.

The WWIII was implemented on the Indian Ocean with a mosaic of two domains (Table 1). In this study area, Amrutha et al. (2016) examined the sensitive analysis of the WWIII by calibrating and validating the difference source terms. Following their recommendation, the model was executed using ST4 physics for the present observation. Bathymetry and obstruction grid files for the selected domains were extracted in the GRIDGEN of version 3 (Chawla and Tolman 2007) by considering full resolution ETOPO1 (Amante and Eakins 2009). Two dimensional (2D) spectra extracted from 1 February 2008 to 31 January 2011 in the mosaic approach of WWIII were used as the offshore boundary to the SWAN for simulation of nearshore surface gravity waves, while the SWAN run was based on the mosaic of two domains (Table 1). The bathymetry data referred in the SWAN model was extracted from Chart No. 2008 of the NHO. The SWAN model setup, the active physical processes, and the initial, as well as boundary conditions, were similar to those described in the earlier observation (Dora and Kumar 2015).

2.3. Numerical approximation

In response to the depth-induced breaking waves those belong either in intermediate or shallow water, the waves were sorted out in which the water depth (d) must be smaller than half of the respective wave length (L). Horikawa (1988) reported that the gamma varies from 0.8 to 1.0 for the spilling breaker, 1.0 to 1.2 for the plunging breaker, and just above 1.2 for the collapsing breaker, whereas the limit was unknown for the surging breaker. The study region is usually dominated by

spilling and plunging waves. Thereby, following the concept derived by Battjes and Janssen (1978) as well as Battjes and Stive (1985), the γ and α were considered as 0.73 and 1 respectively to get most possible breakers. Further, the breakers were classified as spilling ($\xi_b < 0.4$), plunging ($0.4 < \xi_b < 2.0$), surging, or collapsing ($\xi_b > 2.0$) based on the surf similarity parameters derived by the Iribarren number (ξ_b), as given in Eq. (2).

$$\xi_b = \frac{m_b}{\sqrt{H_b/L_0}} \quad (2)$$

where H_b is breaking wave height, L_0 is deep water wave length, m_b is bed slope.

In response to understanding the function of breakers, the mean longshore current (hereafter longshore current) was estimated using the formulae of Longuet-Higgins (1972) and Galvin (1987) which vary in their input parameters as given in Eqs. (3) and (4).

$$v_L = \frac{5.17 \gamma m_b [g H_b]^{0.5} \sin(2\theta)}{16 C} \quad (3)$$

$$v_G = K_G g m_b T \sin[2\theta] \quad (4)$$

where, v_L is mean longshore current (m/s) by Longuet-Higgins (1972), v_G is mean longshore current by Galvin (1987), g is acceleration due to gravity, C ($=0.01$) is coefficient of bottom friction, θ is relative angle of incident wave to depth contour at breaking, K_G ($=1$) is dimensionless coefficient.

The longshore sediment transport (LST) associated with the breaking waves, beach morphology and sediment characteristics was calculated based on the Coastal Engineering Research Center (CERC 1984) and Kamphuis (2013) formulae. Based on the CERC (1984), the total bulk volume LST Rate (LSTR) in m^3/s is:

$$Q_{CERC} = \frac{K}{16 \left(\frac{\rho_s - \rho}{\rho} \right)^{[1-p]}} \sqrt{\frac{g}{\gamma}} H_b^{\frac{5}{2}} \sin [2\theta] \quad (5)$$

where, ρ is water density (1025 kg/m^3), ρ_s is sediment density (2650 kg/m^3), K ($=0.39$) is an empirical coefficient that associated with H_{sig} (SPM 1984), p is sediment porosity, γ is breaker index that has been typically considered as equal to 0.73. Porosity (p) was estimated based on the coefficient of uniformity following Vukovic and Soro (1992) as given in Eq. (6).

$$p = 0.255 * [1 + 0.83^{Cu}] \quad (6)$$

The coefficient of uniformity (Cu) was calculated as $Cu = D_{60}/D_{10}$, where, the D_{10} , and D_{60} are the grain diameter at the tenth and sixth percentages in the cumulative frequency curve of distributed grains.

Based on Kamphuis (2013), the total LSTR (m^3/h) is:

$$Q_K = 7.3H_b^2 T_p^{1.5} m_b^{0.75} D_{50}^{-0.25} \sin^{0.6}[2\theta_b] \quad (7)$$

where, T_p is peak wave period (s), and D_{50} is median grain diameter (mm).

2.4. In situ observation

In situ wave data was collected in deep as well as in coastal zone to validate the simulated waves. The wind data was measured by the Automatic Weather Station (AWS) at near shore and used to validate the reanalysis wind dataset. As the AWS wind was measured at 50 m elevation from MSL, the AWS wind data was converted to 10 m elevation with respect to MSL using Eq. (1). The offshore and nearshore waves were measured by wave rider buoys deployed at 15 m water depth (OWB) and at 7 m water depth (NWB) (Figure 1). The procedure for collection and analysis of wave and wind parameters were as explained in the earlier study (Dora and Kumar 2015). Deep ocean waves measured by deployed wave buoy at AD02 were also used. By deploying an InterOcean S4 directional wave measuring instrument (hereafter S4DW) at surf zone, the waves and current in the surfzone were measured at 1 m water depth. The S4DW is a spherical shape with 25 cm diameter and a weight of 1.5 kg in water. The instrument senses wave orbital current components, and depth sensor provides 4 mm depth resolution. Simultaneously, the S4DW measures the magnitude of current speed following Faraday's law of electromagnetic induction, where two orthogonal pairs of titanium electrodes and an internal flux-gate compass provide the current vector. The meteorological convention is used for the presentation of wind and wave direction (0° for wave/wind from the north, 90° for east, 180° for south, and 270° for west). Measurements were made in Coordinated Universal Time (UTC) and the local time (Indian Standard Time) is 05:30 hrs ahead of UTC.

Earlier observation exhibited that the inter-tidal beach slope varied from 0.62 to 7.32° during the period of three years, and the mean grain size varied between 0.141 and 0.599 mm along the study area (Dora et al. 2012, 2014). The details procedure of collecting sediment characteristics and cross-shore profiles were as explained in earlier studies (Dora et al. 2012, 2014). These data were used to interpret the sediment transport by the Kamphuis approximation (2013). The LSTR measured using sediment trap (S.Trap) in the surfzone by Kumar et al. (2003) was used to determine the accuracy in the estimated LSTR. A brief description of the in situ wind, wave, current, and sediment transport observation used in the study is given in Table 2. As the river discharge data could not be

collected, the analysis was carried out with some limitation in which the river influence was omitted. The reanalysis wind dataset, modelled waves, as well as the estimated alongshore current and the LSTR were compared, and evaluated with respect to field-measured data based on the correlation coefficient (R) and BIAS (B).

3. Results and discussions

3.1. Sea surface wind

The reanalysis wind data was compared with the in situ measurements in the coastal zone over four months (Figure 2). The measured wind data basically belongs to the monsoon and post-monsoon periods. During this period, the maximum wind speed measured by the AWS was 10.7 m/s with an average of 2.9 m/s. The wind rose diagram as well as the time series plot showed that the wind speed having more than 4 m/s was frequently occurring while the wind was from southwest-west (240-270°). The duration as well as the strength of wind decreased gradually towards the north (Figure 2). The time series plot exhibited that the wind from southwest-west was during July and August, whereas the wind was blowing from random direction with comparatively low wind speed (< 4 m/s) during most of the time in September and October. The random wind direction reflects the impact of local wind pattern over the wind propagating from a remote area.

As per the time resolution of wind data, the NCEP/CFSR wind is compared with the AWS wind using 1, 3, and 6 h interval data, however, the degree of agreement of the ECMWF and NCEP/NCAR wind to AWS wind was estimated based on 6 h interval data. The study exhibited that the correlation of NCEP/CFSR wind speed and AWS wind data was almost similar in the data set of different time intervals. The R was 0.48, 0.47, and 0.46, whereas the B was -1.01, -1.04, and -0.99 m/s at 1, 3, and 6 h interval data set respectively. Thereby, all the three reanalysis wind was compared to AWS wind data at 6 h interval. All of the reanalysis wind speed to the AWS wind speed exhibited a moderate correlation while the deviation of reanalysis wind speed from the AWS wind was comparatively more in the NCEP/NCAR wind data (Table 3). However, the wind rose diagram showed that there was a considerable deviation in the reanalysis wind direction from the AWS data, whereas the NCEP/CFSR wind direction showed comparatively closer to the direction of AWS wind. Consequently, further analysis was carried out based on the zonal (x-component/u-component) and meridional (y-component/v-component) wind components. During the period of wind measurement, the zonal component in the AWS wind was between -1.9 and 13.4 m/s with an average value of 2.3

m/s, while the meridional component varied from -9.1 to 6.1 m/s with an average speed of -0.3 m/s. The wind exhibited a good correlation in the zonal component compared with the result observed in the meridional component. The correlation coefficients in the zonal component of the NCEP/CFSR, ECMWF, and NCEP/NCAR wind to the AWS data were 0.67, 0.69, and 0.64, respectively, while they were 0.41, 0.32, and 0.29 in the meridional component. The shoreline inclination is along south-north direction, and hence the coastal breeze dominated to the coast along east-west direction. Hence, the zonal component showed comparatively good correlation between the observed and reanalysis wind data set. Thus, the reanalysis wind direction was poorly correlated to the measured data while the correlation in the wind speed was reasonable.

3.2. Surface gravity waves

3.2.1. Deep and intermediate waves

The analysis was continued for simulating nearshore waves as the earlier study showed that the coast is dominated by swell (Dora and Kumar 2015). The surface gravity waves over the Indian Ocean were simulated using the WWIII model forced by all three sources of wind data (NCEP/NCAR, ECMWF, and NCEP/CFSR). The significant wave height (H_{sig}), peak period (T_p), and associated direction (D_p) was examined in deep ocean as well as in coastal zone by comparing the simulated values with measured data (Figure 3). The number of available data varies from deep ocean to coast, and the correlation coefficients and bias were estimated based on the available data set (Table 2). During most of time, in the deep ocean (Figure 3a) as well as in the nearshore zone (Figure 3b), the simulated wave parameters with the NCEP/CFSR and ECMWF wind were found to be close to the measured wave than the NCEP/NCAR wind simulated wave. From the deep ocean to nearshore zone, an overestimation was observed in the NCEP/NCAR wind-based wave parameters. However, the wave height based on the ECMWF and NCEP/CFSR wind was very close to the time series trend of measured data. Along the three observation points from the deep ocean to nearshore zone, the correlation coefficient (R) in wave height between the NCEP/NCAR forced wave and measured data was 0.895 ± 0.055 and the bias (B) was 0.31 ± 0.22 m, whereas the correlation coefficient between the ECMWF forced wave and measured data was 0.895 ± 0.085 , and the bias was 0.075 ± 0.055 m (Table 4). However, a comparatively good correlation coefficient ($R = 0.93 \pm 0.04$ and $B = 0.04 \pm 0.05$ m) was observed between the NCEP/CFSR forced wave and measured data. The negative bias (-0.01 m) in H_{sig} at the offshore zone exhibits a slight underestimation by the NCEP/CFSR wind, which is

comparatively less than that observed by the ECMWF wind. Earlier, Akpinar et al. (2012) also reported that ECMWF wind underestimate in the simulation of surface wave, whereas, Chawla et al. (2013) and also Van Vledder and Akpinar (2015) found the best result by NCEP/CFSR wind. Correlation of the simulated wave periods based on all the wind sources to the measured data was less than that observed in the H_{sig} . From the deep ocean to nearshore zone, the correlation coefficient in wave period between the NCEP/NCAR wave and measured data was 0.49 ± 0.20 and the bias was 0.31 ± 0.59 s, which reflects a slight overestimation of the simulated wave period. Correlation coefficient of the simulated wave period based on the ECMWF to measured data was -0.545 ± 0.075 , while the negative bias (-0.30 to -0.69 s) exhibited an underestimation of the simulated wave periods. However, for the simulated wave period based on the NCEP/CFSR wind data was found to be better than that observed in the NCEP/NCAR and ECMWF wind data. Correlation coefficient between the NCEP/CFSR simulated wave period and measured data was 0.555 ± 0.085 and bias was 0.085 ± 0.055 s. Further, the study exhibited that the direction of the simulated deep ocean waves based on all wind sources exhibited as almost similar, and they were close to the observational data. Correlation coefficient of the simulated wave direction by the NCEP/NCAR, ECMWF, and NCEP/CFSR wind to the in situ measurement was 0.68, 0.72, and 0.71, and the respective bias was 4.46, 7.25, and 4.69°. The simulated wave directions in the nearshore zone were also found to be reasonable. Correlation coefficient of the wave direction by the NCEP/NCAR, ECMWF, and NCEP/CFSR wind to the measured data were respectively 0.43, 0.60, and 0.44, while the bias was 6°, 7°, and 10°. However, the offshore wave direction during the short period (~10 days) based on all the wind sources showed a poor correlation to the in situ measurement data as the observation point was very close to the offshore islands, where the maximum bias was 10° (Figure 3c).

Earlier analysis revealed that the nearshore intermediate wave simulated using the SWAN model based on 1D wave spectra along the offshore boundary is unrealistic, whereas the simulated waves were reasonable based on the parametric boundary condition (Dora and Kumar 2015). In this study, the coastal wave parameters were again examined using the SWAN model nested by the 2D wave spectra along the offshore boundary. The 2D wave spectra were generated from the WWIII model forced by wind from different sources (Figure 3d). The pictorial presentation of time series wave data exhibited an overestimation in the hindcasted wave height that based on the NCEP/NCAR 2D wave spectra of WWIII. Also, comparatively more deviation was observed in the simulated wave direction from the field measured data, while the wave simulation is based on the NCEP/NCAR wind. Further, the study exhibited that the correlation coefficient in the wave height based on the NCAR/CFSR wind to the measured data was better ($R=0.93$) than that based on the ECMWF wind

($R=0.83$). Additionally, the bias exhibited an underestimation of the simulated wave height by the ECMWF, whereas an overestimation was observed by the NCEP/CFSR. Based on both R and B , the simulated wave period by the NCEP/CFSR was found closer to the measured data ($R = 0.49$, $B = -0.08$ s) than that observed by the ECMWF ($R=0.49$, $B= -0.47$ s), while the simulated wave period by the NCEP/NCAR also exhibited a good correlation ($R = 0.65$, $B = -0.43$ s) to the measured data as compared to the ECMWF. The correlation was poor for the wave direction ($R<0.3$) from all three different wind sources because the deviation of wave direction is a circular pattern, whereas the bias (B) was 8, 7 and 9° for NCEP/CFSR, ECMWF and NCEP/NCAR wind respectively. Also, the earlier observation between the simulated wave direction based on the parametric boundary condition and observation wave data exhibited the bias of 6° while the correlation coefficient was poor (Dora and Kumar 2015). The present study revealed that the nearshore wave parameters can be simulated using the SWAN model either by providing the parametric wave condition or 2D wave spectra along open boundary, whereas the 1D wave spectra were found to be unrealistic. Followed by these statistical analyses as well as the better spatio-temporal resolution among the three reanalysis wind sources, the NCEP/CFSR wind was found to be reasonable overall compared to the NCEP/NCAR and ECMWF wind for the simulation of surface gravity waves in the coastal zone. Hence, depth-induced breakers were simulated in the SWAN nested by the 2D wave spectra obtained from WWIII forced by the NCEP/CFSR wind.

3.2.2. Breaking waves

The breaking waves, extracted from the simulated nearshore waves, were compared with the field measurement over 302 pairs of data collected at 3 h intervals by the S4DW near the BM1 location. During the observation period, the average H_{sig} , T_p , and D_p of the simulated breaking waves were 0.49 m, 11.7 s, and 263°, while the observed data showed 0.47 m, 11.3 s, and 257°. Hence, the simulated breaking waves were considered reasonable. Study showed that the breakers were varying from spilling to plunging nature (Table 5). The spilling breakers were comparatively more at the island sheltered zone (BM2) while the open and partial open coasts (BM1 and BM3) were dominated by plunging breaker. Further, the plunging breakers were gradually decreased with increased spilling breakers from Kali river mouth to Karwar headland along RT beach. This represents the behavior of breakers is highly depend on the wave propagation to the coast, where a typical observation on the

wave propagation and transformation was analyzed earlier followed by eight different case studies (Dora and Kumar, 2015).

Along the WCI, the depth-induced breaking waves along the open coast strongly follow seasonal variations (Shanas and Kumar 2014). In the present study, the breaking waves in the island sheltered zone also exhibited a seasonal pattern followed by the seasonal behavior of the nearshore waves which was observed in the earlier study (Dora and Kumar 2015). Figures 4 and 5 represent the monthly average of the simulated H_{sig} carried out during the three years from February 2008 to January 2011. The breaking waves were energetic during the monsoon, and during the remaining period that was weak. The peak condition of the breaking waves was during July at the open coast as well as at the island and headland sheltered zones, as the extreme rough condition of the monsoon climate along the WCI occurs during the same period (Rajeevan et al. 2010). Further, the behavior of breakers varies along the shore due to non-uniform coastal morphology along the locations.

The three locations (BM1, BM2, and BM3) along the Devbag beach exhibited considerable variation in the breaking waves. The BM1 location was partially blocked by Kurmagadgudda Island from the SW waves, which is the dominant direction of waves along this region (Dora and Kumar 2015). During most of the time, the wave propagation to the BM1 location was from 255 to 270° as a result of the refraction and diffraction phenomena while the SW waves propagate to the coast. The wave height at this location was up to 2.5 m, and the high waves (2-2.5 m) occurred during the monsoon. The BM2 location was fully sheltered by the nearshore islands of Kurmagadgudda and Shimisgudda. The earlier study revealed that the high energy waves during the monsoon were almost orthogonal to the coast in a narrow range in terms of frequency and direction (Dora and Kumar 2015). Hence, the location BM2 is protected from high-intensity direct waves. Thus, this location was dominated by waves reaching from 225 to 240° , where the wave height was up to 1 m during most of the time. The waves from 240 to 300° were the result of interference between the waves diffracted due to the nearshore islands, as the location is obstructed by the nearshore islands from the direct waves approaching in this sector. The average wave height at this location was 0.8 m, and the maximum wave height was 2.1 m during the monsoon. The BM3 location was blocked by nearshore as well as offshore islands from southwest-west waves. Also, the depth contours from 5 m to the shoreline were strongly tilted towards the west from the true north. Hence, the breaking waves at this zone represent SW waves, where the waves from 225 to 240° were dominated in this zone with a maximum height of 2.4 m. Following the classification of Bromirski et al. (2005), the breaking waves along these three locations were mainly observed as intermediate ($6 < T_p < 12$ s) and long period ($T_p > 12$ s) waves, while the short period ($T_p < 6$ s) waves occurred rarely from 225 and 240° ,

and comparatively more of them were observed at BM2 and BM3. The short period waves at BM1 were comparatively less, and these were from 255 and 270°, which was the result of diffraction by the nearshore islands on the waves from 225 to 240°. The overall study shows that the breaking zone at Devbag beach was dominated by intermediate and long period waves (Figure 4). The breaking waves along the three locations at Devbag beach revealed that the nearshore islands play a major role in the variation of breaking wave intensity and behavior.

Along the locations from BM4 to BM6 on the RT beach, the number of high waves decreased gradually with a clockwise shift of the wave direction from the SW to the northwest-west ($270 < D_p \leq 300^\circ$). At the BM4 location, most of the breaking waves were from the SW, while the breaking waves at the BM5 location were from the southwest-west and northwest-west directions. The maximum H_{sig} at the BM4 location was 3 m, whereas it was 2.5 m at the BM5 location and both of these peak wave heights occurred during the monsoon. The breaking waves at the BM6 location were dominated by the waves from the northwest-west direction in which the maximum H_{sig} was 1.4 m and are mainly observed during the monsoon. The gradual clockwise shift of the wave direction from the BM4 to BM6 locations was due to the presence of the Karwar headland, which blocks the SW waves. The breaking waves at the BM4 and BM5 locations were the result of intermediate and long period waves, whereas the breaking waves at the BM6 location exhibited a considerable quantity of short period waves along with intermediate and long period waves (Figure 5). About 75% of the short-period waves at the BM6 location indicate that the wave climate at this location was dominated by the local wind condition, where the H_{sig} in 90% of the data was less than 1 m. The study found that, even though BM1 and BM6 locations were open to northwest waves, short period waves were observed only at the BM6 location. This is due to the poor contribution of the swells in the resultant waves at the BM6 location, whereas the swell effect is considerable at BM1 location. Further, the study revealed that the waves at the breaking zone during an annual cycle were spatio-temporally bi-directional (SW and NW), where overall, the H_{sig} was less than 1 m. The study on breaking wave behavior from BM1 to BM6 in the island sheltered coastal zone revealed that the wave behavior at breaking zone can be different from that of the source wave, and hence observation on the offshore wave apart from the nearshore zone is essential for studying the coastal processes.

3.3. Longshore current

Followed by the examination of breaking wave formation, the alongshore current was analyzed at all six locations. Based on the input parameters, there is some difference between the concept of Longuet-Higgins (1972) and Galvin (1987) which was considered in this study for estimating the alongshore current. The concept derived by Longuet-Higgins is proportional to the breaking wave height, whereas Galvin reported that the alongshore current was strongly proportional to the wave period while the role of the wave height is negligible. However, both of these formulations depend on the beach slope and angle of the wave approach to the coast (relative angle). Thereby, the alongshore current was evaluated based on both the concepts. The results were examined by comparing the field data measured using S4DW, where the measured breaker parameters were used as input to the formulae for estimating alongshore current. During measurement period in the surfzone, the maximum wave height (H_{max}) varied from 0.38 to 1.55 m and the H_{sig} was between 0.24 and 0.94 m. Simultaneously, the predominant wave direction (D_p) was $241 \pm 45^\circ$. Total 302 data set, collected in the breaking zone, exhibited that the maximum wave height was 1.64 times to the significant wave height, while the peak period (T_p) was 1.98 times to the significant wave period (T_s), 2.35 times to the zero-crossing wave period (T_z), and 3.81 times to the crest period (T_c). The average alongshore current measured by the S4DW was 0.08 m/s with a maximum value of 0.38 m/s. Using these measured breaking wave parameters, an overestimation was observed in the estimated alongshore current based on the Longuet-Higgins formula. The estimated average alongshore current was 1.14 m/s, while the average H_{sig} was 0.47 m, the average angle of the wave approach to the coast was 15° , and the beach slope from the waterline to the position of S4DW was 1:55. Further, Longuet-Higgins reported that the alongshore current observed in field and laboratory experiments is consistent with a friction coefficient (C) of about 0.01 while horizontal mixing was taken into account. Hence, the Longuet-Higgins concept was not considered for further study due to the poor performance in the estimation of alongshore current, and also there is no tuning factor other than the friction coefficient. Thereby, the Galvin approximation was examined for estimating alongshore current. As the wave period in the Galvin formula is directly proportional to the alongshore current, the usage of peak period (T_p) will estimate highest alongshore current, whereas the crest period will estimate lowest alongshore current. The Galvin formula using the crest period exhibited a slight overestimation in the predicted alongshore current, and it was found to be more reasonable than the value based on the other wave periods. Thus, a further modification was taken in the dimensionless coefficient (K_G), whereas Galvin observed a range in K_G such as the lower value (0.6) for field observation and the higher value (1.1) for laboratory conditions. The estimated average alongshore current was observed as 0.11 m/s by the Galvin formula using the crest period and $K_G=0.6$, and the

maximum alongshore current was 0.37 m/s, which are closer to the measured data. Thereby, alongshore current was estimated by the Galvin formula at all the locations (Figure 6) based on the crest wave period. Analysis showed that the magnitude of the alongshore current at a particular location strongly depends on the variation of either the angle of the wave approach to the coast or the wave period.

The relative angle was observed in a wider range, whereas the wave period was almost similar at all the locations (Figure 6). The diversity of relative angle was observed considerably at the island (BM2) and headland (BM6) sheltered zones. Annual average (range) relative angle at both the locations showed southward direction, and these were respectively -12° ($0\pm 44^\circ$) and -13° ($0\pm 38^\circ$). Annual average (range) relative angle at the remaining four locations were towards the north direction, and these were 6° ($13\pm 15^\circ$), 5° ($7\pm 34^\circ$), 8° ($10\pm 17^\circ$), and 2° ($7\pm 8^\circ$) respectively at the BM1, BM3, BM4, and BM5 locations. The annual maximum crest period (T_c) along the six locations was 6 s, whereas the annual average crest period (T_c) was 3 s from BM1 to BM5, and that was 2 s at BM6 locations. Consequently, the annual average alongshore current at BM2 and BM6 was southerly, and that was -0.06 and 0.04 m/s respectively. The annual average alongshore current at the remaining locations was 0.13, 0.01, 0.05, 0.03 m/s respectively at the BM1, BM3, BM4, and BM5 locations. The maximum alongshore current was towards the north, and that was 0.50, 0.22, 0.18, 0.24, 0.16, 0.05 m/s respectively from BM1 to BM6. The study showed that the role of relative angle on alongshore current was strong in the island and headland sheltered zones (BM2 and BM6), whereas it was weak along the open coast (BM5). Further, the study exhibited that the annual maximum, as well as average wave crest period, was almost similar from BM1 to BM5 due to the swell dominant area, whereas the dominance of wind-sea reduced the wave crest period at BM6 location. At all the locations, a seasonal variation in the alongshore current was observed. During the monsoon, the alongshore current at the island/headland sheltered zone (BM2 and BM6) was strong due to the high relative angle. However, a reversal pattern was observed in the seasonal occurrence of the alongshore current at the BM1 location. A weak alongshore current at BM1 during the monsoon was due to the low relative angle, whereas that was comparatively high during the non-monsoon period. The alongshore current was strong (maximum of 0.5 m/s) at the BM1 location, where the wave period as well as relative angle together plays a major role than that observed at the other locations. During the annual cycles, based on the computed value, the study showed that the maximum northward alongshore current at Devbag beach was 2 times to that estimated at RT beach, whereas the maximum southerly alongshore current was almost similar. The annual average of alongshore current at both the beaches exhibited a dominance of northward alongshore current.

3.4. Longshore sediment transport

The CERC (1984) and Kamphuis (2013) formulae, considered in this study for estimating the LSTR, strongly differ from each other based on their input parameters. The CERC formula depends on the breaking wave height, whereas the grain size, wave period, and beach slope contribute considerably in the Kamphuis approximation. The angle of the wave approach to the coast plays a major role in both of the approximations. The degree of agreement of these two formulae for estimating the LSTR was analyzed by comparing the sediment transport data collected in the field using sediment trap. At the sediment transport measurement location, the surfzone width was 40 ± 10 m, and the range of the grain size was 195 ± 45 μ m. Based on the observed data, the average LSTR was $230 \text{ m}^3/\text{day}$, while the average breaking wave height and peak period was 0.87 m and 11 s, respectively, and the average relative angle of the wave approach to the coast was 4.9° (Kumar et al. 2003). The field measured parameters revealed that the LSTR based on the CERC formula was $944 \text{ m}^3/\text{day}$, whereas the Kamphuis approximation showed $279 \text{ m}^3/\text{day}$, which was closer to the measured data ($230 \text{ m}^3/\text{day}$). As K is the only tuning parameter in the CERC formula, the range of K was taken instead of a constant following the derivation of King (2005), who suggested a simple relation of K to the size of grain diameter [D_{50}] as given in Eq. (11).

$$K_{sig} = \frac{R_D}{D_{50}} \quad (11)$$

where D_{50} is the size of grain diameter (mm) and R_D ($=0.1$ mm) is the reference grain size that is constant in space and time. The Eqs. (5) and (11) together with constant porosity ($p=0.43$) represents the modified form of the CERC formula as given in Eq. (12).

$$Q_{CERC} = \frac{0.0069}{D_{50}} \sqrt{\frac{g}{\gamma}} H_b^{\frac{5}{2}} \sin [2\theta] \quad (12)$$

It is clear that the modified CERC formula, i.e. Eq. (12), will increase the LSTR in case of finer grains ($D_{50} < 0.26$ mm) than the predicted LSTR by the original CERC formula with $K = 0.39$. However, the predicted LSTR will be reduced in cases of medium ($0.25 < D_{50} < 0.5$ mm) and coarse ($0.5 < D_{50} < 1$ mm) grains. Thus, the estimated LSTR based on the modified CERC formula was overestimated as the size of grain diameters of all the samples was less than 0.2564 ($=0.1/0.39$) mm. This revealed that the concept of King (2005) for estimating LSTR with the help of CERC (1984) is applicable to some specific sedimentary environment. However, the size of grain diameter along the

Karwar shoreline was observed a mixture of fine, medium and coarse sands during the three annual cycles. Hence, the LSTR based on the modified CERC formula (Eq. 12) was examined with respect to the Kamphuis approximation at the different breaking zones having their unique morphology.

The estimated LSTR based on both approximations exhibited a uniform trend and strong seasonal variation at all the six locations (Figure 7). To obtain both the net sediment transport (ST_{net}) as well as the gross sediment transport (ST_{gross}) for each month, the LSTR was estimated at hourly intervals followed by the estimated breaking wave parameters, where the beach slope, median grain size, and porosity were unchanged during the monthly interval. Most of the time, the net sediment transport was strongly northward except at the island and headland sheltered zones (BM2 and BM6), and it showed a similar result to that observed in the alongshore current. The ratio of LSTR based on the modified CERC formula to the Kamphuis approximation was 4, 21, 5, 8, 12, and 28, respectively, at the BM1, BM2, BM3, BM4, BM5, and BM6 locations. This observation showed that the degree of accuracy in the predicted LSTR by the modified CERC formula gradually decreases from the open coast to the sheltered zone. Thereby, the study revealed that the morpho-sedimentary characteristics of a beach are essential for estimating the LSTR. Further, the earlier observations (Dora et al. 2012, 2014) found that there was no strong correlation between the grain size and beach slope at the island sheltered beaches. Hence, the Kamphuis approximation is reasonable for all types of coastal zones since it considers all the responsible parameters. The ST_{gross} was closer to the ST_{net} at all locations except for the BM3 location. This indicates that the sediment transport at the BM1, BM2, BM4, BM5, and BM6 locations were strongly unidirectional during the annual cycle. At the BM3 location, the gross LSTR was 1.7 times the ST_{net} due to the frequent occurrence of the bidirectional longshore sediment transport. The unidirectional sediment transport was observed towards the north at open coast, and that was towards the south at island/headland sheltered zones. Thereby, the monthly observation of the longshore sediment transport (LST) exhibited that July is the peak period when the extreme sediment transport occurred in all types of coastal zones along the Karwar shoreline. Overall, the study predicted that the annual ST_{net} (ST_{gross}) based on the Kamphuis formula during the three consecutive years along the Devbag beach (combined result of BM1, BM2, and BM3) was 0.4×10^5 (1.4×10^5) $m^3/year$. Similarly, the annual ST_{net} (ST_{gross}) along the RT beach (combined result of BM4, BM5, and BM6) was 0.7×10^5 (0.8×10^5) $m^3/year$. At Devbag beach, the study result showed that the relation of gross to net sediment transport was 3.5, while that was 1.1 at RT beach. The gross value exhibited that the LSTR was more at the Devbag beach compared to the RT beach, whereas the Devbag beach with a low net sediment transport is found to be more stable than the RT beach. Earlier, Chandramohan and Nayak (1991) reported that the Karwar coast is

dominated by a bidirectional LST, whereas Kunte and Wagle (2001) observed northerly sediment transport along this coast. The contrasting results between the present study and earlier observations as well as the non-uniform behaviour of sediment transport along the shoreline together show the necessity of long-term observation of sediment transport before planning any coastal protection measures.

4. Conclusion

This study has shown that the NCEP/CFSR wind is reasonable for prediction of surface gravity wave at the sheltered coastal zone. Further, the study revealed that the Kamphuis (2013) formula for estimating sediment transport is realistic from open coast to sheltered zones, whereas the CERC (1984) formula along with the concept of King (2005) overestimates. Galvin's (1987) formula gives a reasonable result in estimation of longshore current compared to that based on Longuet-Higgins (1972). Observation on the function of breaking waves, the longshore current and sediment transport, revealed that the information about beach morphology and sediment characteristics is essential along with breaking wave parameters for the interpretation of beach stability. The study area, Karwar - the island sheltered coast, was observed as having spilling and plunging breakers based on Iribarren's surf similarity parameter. The associated longshore current and sediment transport were observed bi-directionally along the shore due to complex morphology, whereas both of them exhibited net northward direction in an annual cycle. Observation revealed that the physical processes in the breaking zone along a sheltered coast are under strong dynamics due to its complex bathymetry and hence, long-term observation along the shoreline is essential.

Acknowledgement: We thank ICMAMPD, Ministry of Earth Sciences, New Delhi, for partially funding the measurement program. Director, CSIR-NIO, Goa, and Project Director, ICMAM PD, Chennai, for the encouragement provided to carry out the study. We thank all colleagues for the help provided during the measurement and analysis. The AWS data was provided by Mr. Prakash Mehra, Scientist, NIO, Goa. The deep water buoy data used for evaluation of simulated data was collected by National Institute of Ocean and Technology, Chennai. The first author acknowledges the CSIR for the financial support as senior research fellowship. This publication is a NIO contribution, and forms a part of the PhD thesis of first author.

References

- Akpınar A, Van Vledder GPh, Komurcu MI, Ozger M (2012) Evaluation of the numerical wave model (SWAN) for wave simulation in the Black Sea. *Cont Shelf Res* 50-51:80-99.
- Amante C, Eakins BW (2009) ETOPO1 1arc-minute global relief model: procedures, data sources and analysis. NOAA technical memorandum NESDIS NGDC-24. National Geophysical Data Center, NOAA, doi:10.7289/V5C8276M (12 October 2014).
- Amrutha MM, Kumar VS, Sandhya KG, Nair TMB, Rathod JL (2016) Wave hindcast studies using SWAN nested in WAVEWATCH III – comparison with measured nearshore buoy data off Karwar, eastern Arabian Sea. *Ocean Eng* 119:114-124.
- Babanin A (2011) *Breaking and dissipation of ocean surface wave*. Cambridge University Press, Science.
- Battjes JA, Janssen JPFM (1978) Energy loss and set-up due to breaking of random waves. *Proceedings 16 International Conference in Coastal Engineering, ASCE*. 569–587.
- Battjes JA, Stive MJF (1985) Calibration and verification of a dissipation model for random breaking waves. *J Geophys Res* 90 9159–9167.
- Booij N, Ris RC, Holthuijsen LH (1999) A third generation wave model for coastal regions. Model description and validation. *J Geophys Res* 104:7649–7666.
- Bromirski PD, Cayan DR, Flick RE (2005) Wave spectral energy variability in the northeast Pacific. *J Geophys Res* 110:C03005, doi: 10.1029/2004JC002398.
- CEM (2006) *Coastal Engineering Manual, Chapter II-2, Meteorology and Wave Climate, Engineer Manual 1110-2-1100*, U.S. Army Corps of Engineers. Washington, DC.
- CERC (1984) *Shore Protection Manual, Vols I and II; Coastal Engineering Research Center*. U.S. Army Corps of Engineers, Washington, DC. U.S. Government Printing Office, Vicksburg.
- Chandramohan P, Nayak BU (1991) Longshore sediment transport along the Indian coast. *Indian J Mar Sci* 20:110–114.
- Chawla A, Tolman HL (2007) Automated grid generation for WAVEWATCH III. *Technical Bulletin 254, NCEP/NOAA/NWS, National Center for Environmental Prediction, Washington, DC*.
- Chawla A, Splindler DM, Tolman HL (2013) Validation of a thirty years wave hindcast using the climate forecast system reanalysis winds. *Ocean Model* 70:189-206.
- Chen Q, Zhao H, Hu K, Douglass SL (2005) Prediction of Wind Waves in a Shallow Estuary. *J Waterw Port Coast Ocean Eng* 131:137-148.
- Dee DP (2011) The ERA-Interim reanalysis: configuration and performance of the data assimilation system. *Q J R Meteorol Soc* 137:553–597.

- Dora GU, Kumar VS (2015) Sea state observation in island sheltered nearshore zone based on in situ intermediate-water wave measurements and NCEP/CFSR wind data. *Ocean Dynam* 65:647-663.
- Dora GU, Kumar VS, Johnson G, Philip CS, Vinayaraj P (2012) Short-term observation of beach dynamics using cross-shore profiles and foreshore sediment. *Ocean Coast Manage* 67:101-112.
- Dora GU, Kumar VS, Philip CS, Johnson G (2014) Quantitative estimation of sediment erosion and accretion processes in a micro-tidal coast. *Int J Sediment Res* 29:218-231.
- Faucher M, Burrows WR, Pandolfo L (1999) Empirical-statistical reconstruction of surface marine winds along the western coast of Canada. *Clim Res* 11:173–190.
- Galvin C (1987) The continuity equation for longshore current velocity with breaker angle adjusted for a wave-current interaction. *Coast Eng* 11:115-129.
- Galvin CJr (1972) Wave breaking in shallow water, Waves on beaches. In Meyer, R.E.(ed.), New York, pp. 413-451.
- Hanamgond PT, Mitra D (2007) Dynamics of the Karwar Coast, India, with special reference to study of Tectonics and Coastal Evolution using Remote Sensing Data. *J Coastal Res SI* 50:842-847.
- Horikawa K (1988) Nearshore dynamics and coastal processes: theory, measurement and predictive models; University of Tokyo press, Tokyo.
- Iverson HW (1952) Waves and breakers in shoaling water, gravity waves. Circular 521, National Bureau of Standards, Washington, DC, pp. 1-12.
- Kalnay et al (1996) The NCEP/NCAR 40-year reanalysis project. *Bull Amer Meteor Soc* 77:437-470.
- Kaminsky GM, Kraus NC (1993) Evaluation of depth-limited wave breaking criteria. Proc. of 2nd Int. Symposium on Ocean Wave Measurement and Analysis, New Orleans, pp. 180-193.
- Kamphuis JW (2013) Uncertainty, research, science and engineering in coastal dynamics. *Coastal dynamics* 110.
- King DBJr (2005) Influence of grain size on sediment transport rates with emphasis on the total longshore rate, ERDC/CHL CHENT-II-48. Vicksburg, MS: U.S. Army Engineer Research and Development Center.
- Kumar VS, Anand NM, Chandramohan P, Naik GN (2003) Longshore sediment transport rate-measurement and estimation, central west coast of India. *Coast Eng* 48:95–109.
- Kumar VS, Pathak KC, Pednekar P, Raju NSN, Gowthaman R (2006) Coastal processes along the Indian coastline. *CurrSci India* 91:530-536.
- Kunte PD, Wagle BG (2001) Littoral transport studies along west coast of India – A review. *Indian J Mar Sci* 30:57-64.

- Londhe SN, Deo MC (2004) Artificial neural networks for wave propagation. *J Coastal Res* 20:1061–1070.
- Longuet-Higgins MS (1972) Recent progress in the study of longshore current. In R.E. Meyer (Editors), *Waves on beaches and resulting sediment transport*. Academic Press, New York, N.Y., pp. 203-248.
- Nayak GN (1993) *Beaches of Karwar: morphology, texture and mineralogy*. RajhaunsVitaran, Panjim, Goa, India, pp. 1–194.
- Nelson RC (1997) Height limits in top down and bottom up wave environments. *Coast Eng* 32:247–254.
- Pitman S, Gallop SL, Haigh ID, Masselink G, Ranasinghe R (2016) Wave breaking patterns control rip current flow regimes and surfzone retention. *Mar Geol* 382: 176-190, doi: 10.1016/j.margeo.2016.10.016
- Rajeevan M, Gadgil S, Bhate J (2010) Active and break spells of the Indian summer monsoon. *J Earth SystSci* 119:229-247.
- Roland BS (1988) *An introduction to Boundary Layer Meteorology*. Kluwer Academic Publishers, pp. 666.
- Saha S (2010) The NCEP Climate Forecast System Reanalysis. *B Am MeteorolSoc* 91:1015-1057.
- Schmidt FH (1947) An elementary theory of the land and sea-breeze circulation. *J Meteor* 4:9-20.
- Shanas PR, Kumar VS (2014) Coastal processes and longshore sediment transport along Kundapura coast, central west coast of India. *Geomorphology* 214:436-451.
- SPM (1984) U.S. Army Engineer Waterways Experiment Station. U.S. Government Printing Office, Washington, DC.
- Tissier M, Bonneton P, Marche F, Chazel F, Lannes D (2012) A new approach to handle wave breaking in fully non-linear Boussinesq models. *Coast Eng* 67: 54-66.
- Tolman HL (2014) The WAVEWATCH III Development Group, User Manual and System Documentation of WAVEWATCH III version 4.18. Technical Note 316, NOAA/NWS/NCEP/MMAB, 282 pp. + Appendices.
- Van VledderGPh, Akpinar A (2015) Wave model predictions in the Black Sea: Sensitivity to wind fields. *Appl Ocean Res* 53:161–178.
- Vinayaraj P, Johnson G, Dora GU, Philip CS, Kumar VS, Gowthaman R (2011) Quantitative estimation of coastal changes along selected locations of Karnataka, India: a GIS and remote sensing approach. *Int J Geosci* 2:385–393.
- Vukovic M, Soro A (1992) *Determination of Hydraulic Conductivity of Porous Media from Grain-Size Composition*. Water Resources Publications, Littleton, Colorado.

|

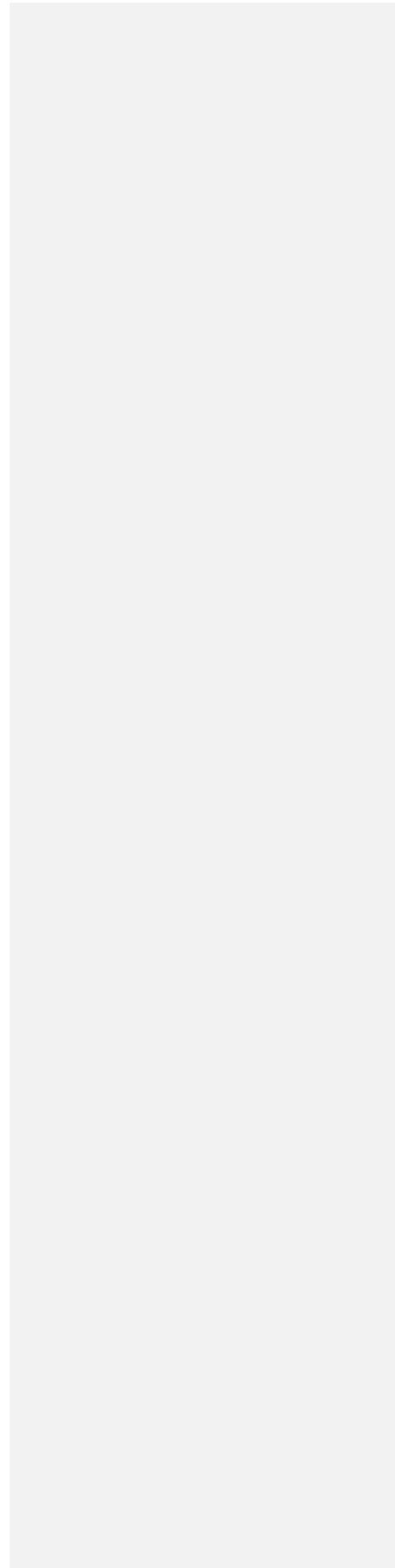


Figure captions:

Figure 1: Pictorial presentation of study area including offshore/nearshore islands, locations of waverider buoys (OWB and NWB), collected sediment samples and monitored cross-shore profiles (BM1 to BM6). The water depth (m) below chart datum is negative.

Figure 2: Wind rose and time series plot of AWS, NCEP/CFSR, ECMWF and NCEP/NCAR wind data at coastal region.

Figure 3: Time series plot of measured wave parameters and that estimated based on NCEP/CFSR, ECMWF and NCEP/NCAR wind data in (a) deep, (b) nearshore (c) offshore, and (d) nearshore. At deep, the estimated values based on WWIII and at other locations are based on SWAN coupled with WWIII.

Figure 4: Breaking wave parameters simulated by NCEP/CFSR wind at three locations (BM1, BM2 and BM3) along Devbag beach. Top panel shows the time series plot of breaking wave height, middle panel shows the wave rose diagram of wave height and bottom panel shows the wave rose diagram of wave period.

Figure 5: Same as Figure 4 for locations along RT beach (BM4, BM5 and BM6).

Figure 6: Time series plot of mean longshore current based on Galvin approximation, wave period based on SWAN simulation, and relative angle at six locations along two beaches during February 2008 to January 2011.

Figure 7: Monthly net (ST_{net}) and gross (ST_{gross}) sediment transport at six locations based on modified CERC and Kamphuis formulae.

Table 1: Brief description of computational domains used in WWIII and SWAN.

Model	Domain outlook			Spherical coordinate			
	Number	Grid	Resolution	Area start (Lat, Lon)	Area end (Lat, Lon)	dx (x-axis)	dy (y-axis)
WWIII	First	Coarse	Low	20.50° E, 59.50° S	149.50° E, 29.50° N	0.50°	0.50°
	Second	Moderate	Medium	73.50° E, 14.00° N	74.50° E, 15.50° N	0.05°	0.05°
SWAN	Third	Fine	High	73.98° E, 14.74° N	74.14° E, 14.86° N	0.001°	0.001°
	Fourth	Very fine	Very high	74.05° E, 14.80° N	74.14° E, 14.86° N	0.0002°	0.0002°

Table 2: Brief description on the in situ wind, wave, current and sediment transport (ST) data used for evaluation of model simulation and numerical estimation (S.Trap indicates sediment trap).

Data	Region	Name	Location (lon, lat)	Time duration		Water depth / land elevation
				(start)	(end)	
Wind	Coastal	AWS	74° 07' 55" E, 14° 50' 48" N	01-07-2009	31-10-2009	50 m
Wave	Deep	AD02	68° 59' 11" E, 15° 0' 22" N			-3500 m
	Offshore	OWB	74° 03' 11" E, 14° 49' 17" N	20-12-2010	30-12-2010	-15 m
	Nearshore	NWB	74° 06' 04" E, 14° 49' 56" N	01-02-2009	14-01-2010	-7 m
	Breaking zone	S4DW	74° 06' 39" E, 14° 51' 11" N	01-09-2008	31-10-2008	-1 m
Current						
ST	Surf zone	S.Trap	74° 08' 29" E, 14° 46' 41" N	04-02-1990	18-05-1990	-2 m

Table 3: Scenario of statistical observation on wind speed (m/s) of NCEP/NCAR, ECMWF, and NCEP/CFSR with AWS measurement.

Statistic	AWS	AWS	AWS
	vs NCEP/NCAR	vs ECMWF	vs NCEP/CFSR
R	0.49	0.62	0.46
BIAS	2.24	-0.71	-0.99

Table 4: Scenario of statical observation on wave parameters of NCEP/NCAR, ECMWF, and NCEP/CFSR with AWS measurement.

Wave parameters	Buoy vs		Buoy vs		Buoy vs	
	NCEP/NCAR		ECMWF		NCEP/CFSR	
	R	BIAS	R	BIAS	R	BIAS
Deep ocean wave (2009)						
Wave height (m)	0.95	0.53	0.98	-0.13	0.97	0.05
Wave period (s)	0.57	0.43	0.62	-0.69	0.64	0.14
Wave direction (°)	0.68	4.46	0.72	7.25	0.71	4.69
Offshore wave (2010)						
Wave height (m)	0.85	0.09	0.81	-0.09	0.89	-0.01
Wave period (s)	0.69	-0.28	0.47	-0.38	0.48	-0.03
Wave direction (°)	-0.13	9.36	0.32	10.15	0.30	10.24
Nearshore wave (2009)						
Wave height (m)	0.84	0.20	0.90	-0.02	0.89	0.09
Wave period (s)	0.29	0.90	0.47	-0.30	0.47	0.13
Wave direction (°)	0.43	5.83	0.60	6.68	0.44	9.91
Nearshore wave (2010)						
Wave height (m)	0.89	0.15	0.83	-0.02	0.93	0.07
Wave period (s)	0.65	-0.43	0.49	-0.47	0.49	-0.08
Wave direction (°)	0.17	8.65	0.01	6.51	-0.05	7.73

Table 5: Breaking wave classification and quantification (%) based on the surf similarity parameters derived by the Iribarren number (ξ_b).

Type	Range	BM1	BM2	BM3	BM4	BM5	BM6
Spilling	$\xi_b < 0.4$	4	76	4	30	40	55
Plunging	$0.4 < \xi_b < 2.0$	96	24	96	70	60	45

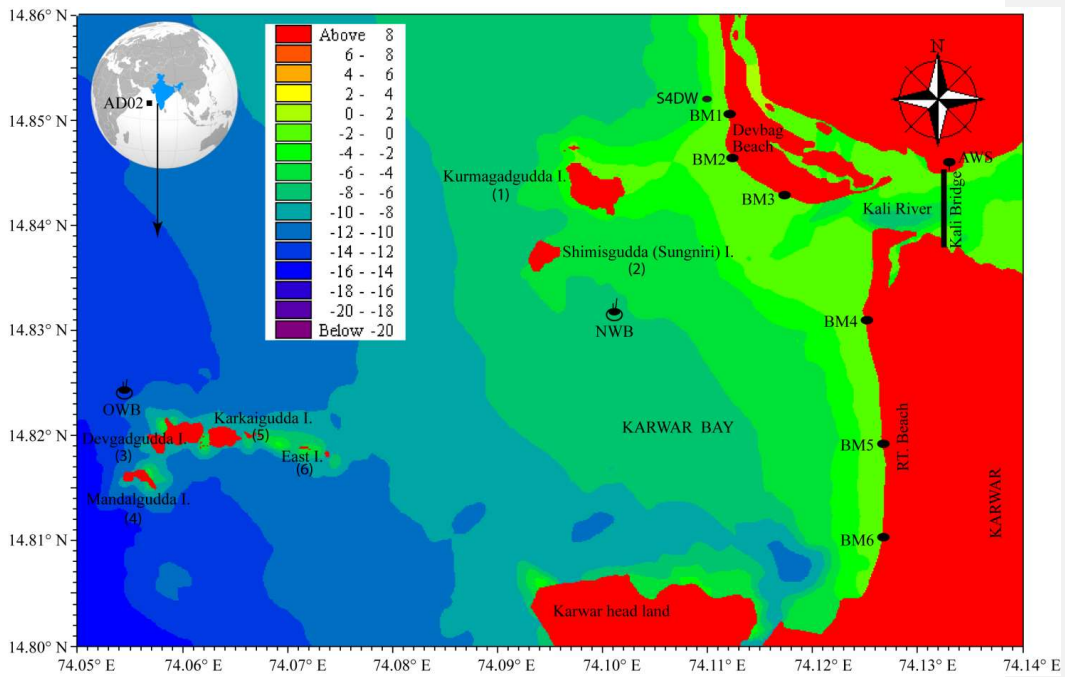


Figure 1: Pictorial presentation of study area including offshore/nearshore islands, locations of waverider buoys (OWB and NWB), collected sediment samples and monitored cross-shore profiles (BM1 to BM6). The water depth (m) below chart datum is negative.

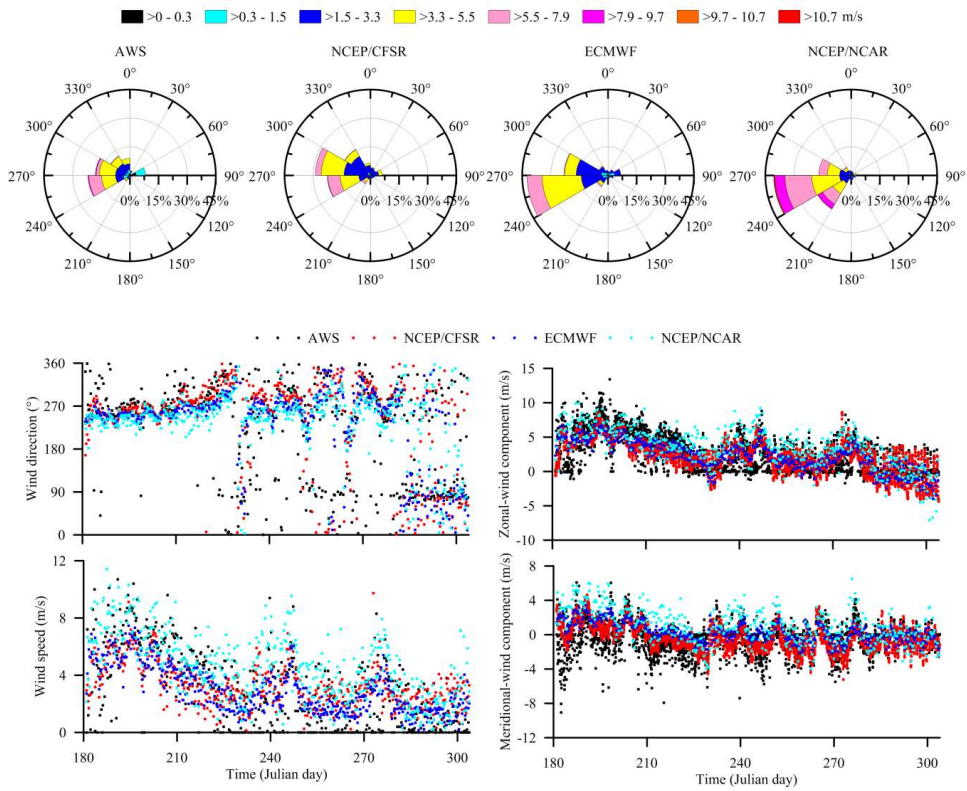


Figure 2: Wind rose and time series plot of AWS, NCEP/CFSR, ECMWF and NCEP/NCAR wind data at coastal region.

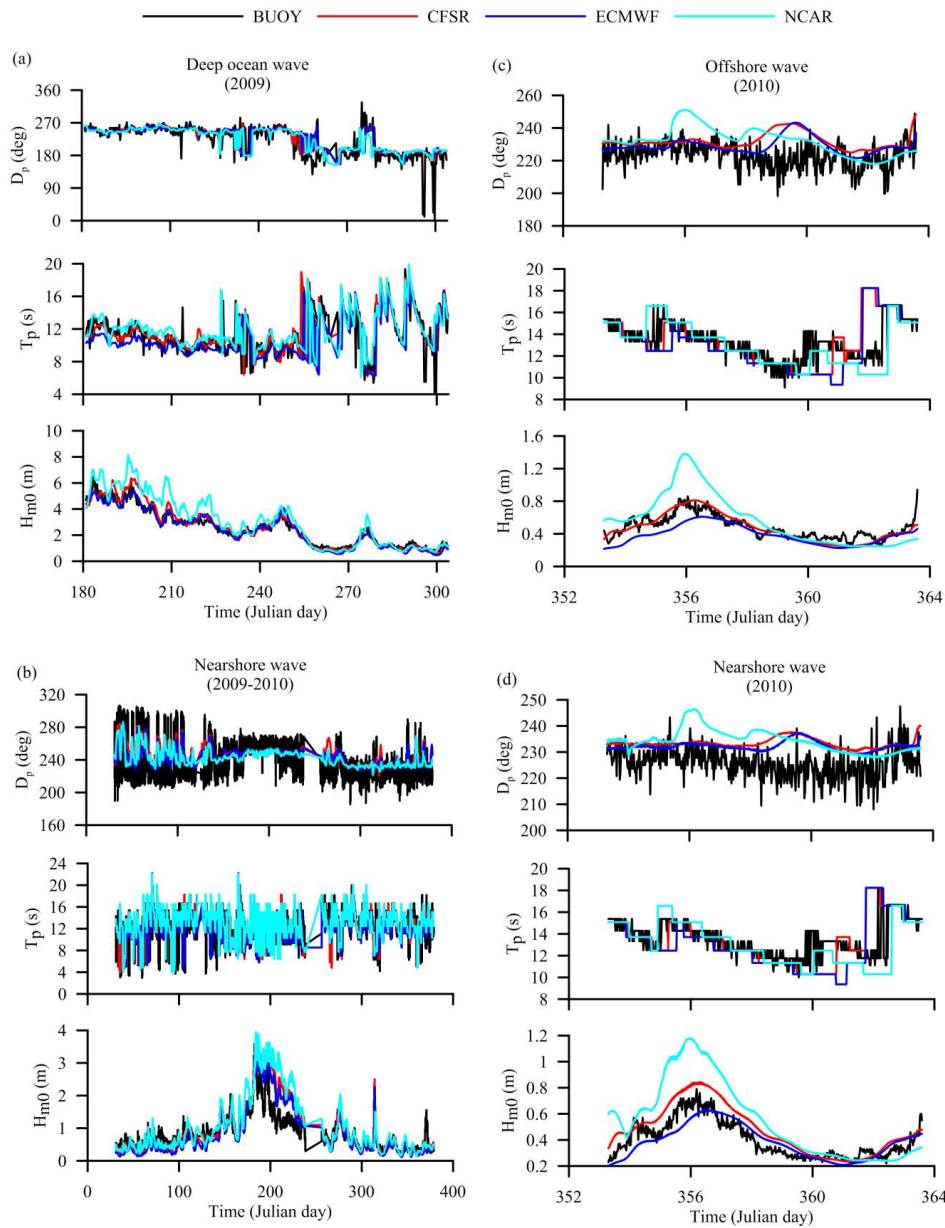


Figure 3: Time series plot of measured wave parameters and that estimated based on NCEP/CFSR, ECMWF and NCEP/NCAR wind data in (a) deep, (b) nearshore (c) offshore, and (d) nearshore. At deep, the estimated values based on WWIII and at other locations are based on SWAN coupled with WWIII.

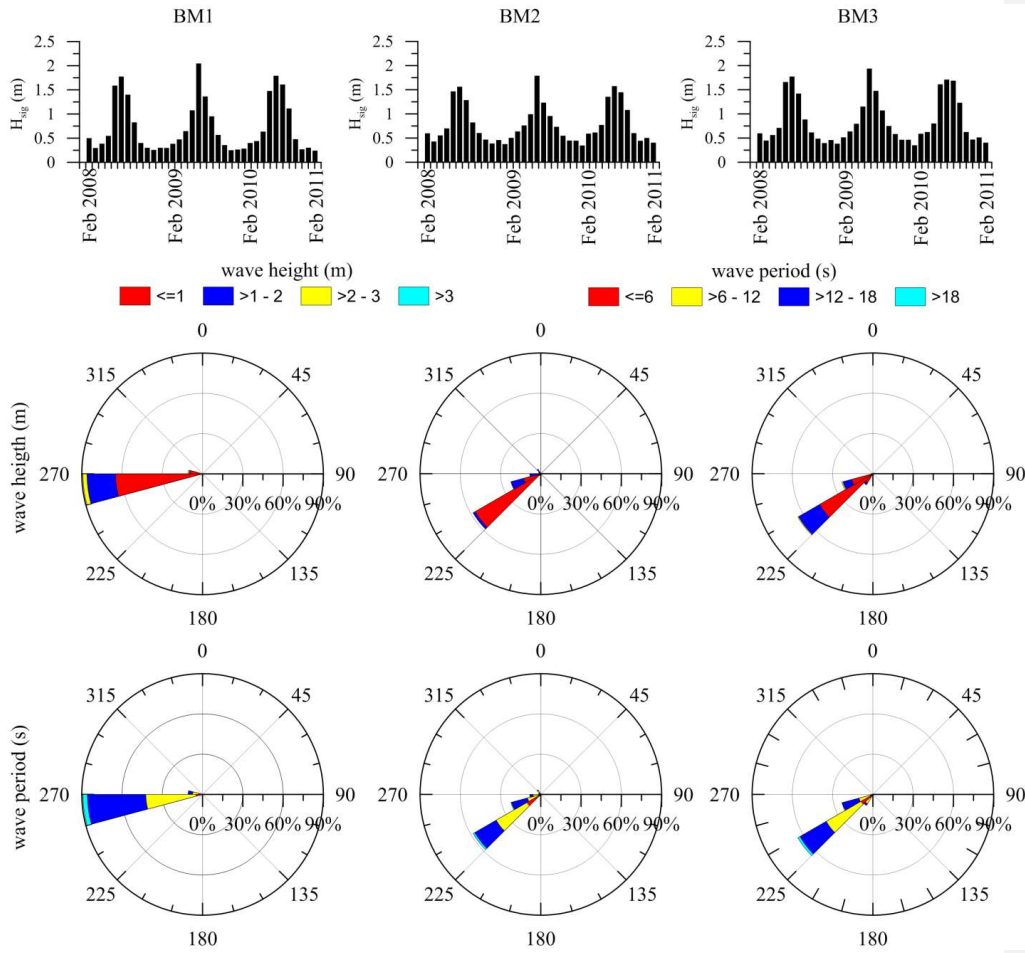


Figure4: Breaking wave parameters simulated by NCEP/CFSR wind at three locations (BM1, BM2 and BM3) along Devbag beach. Top panel shows the time series plot of breaking wave height, middle panel shows the wave rose diagram of wave height and bottom panel shows the wave rose diagram of wave period.

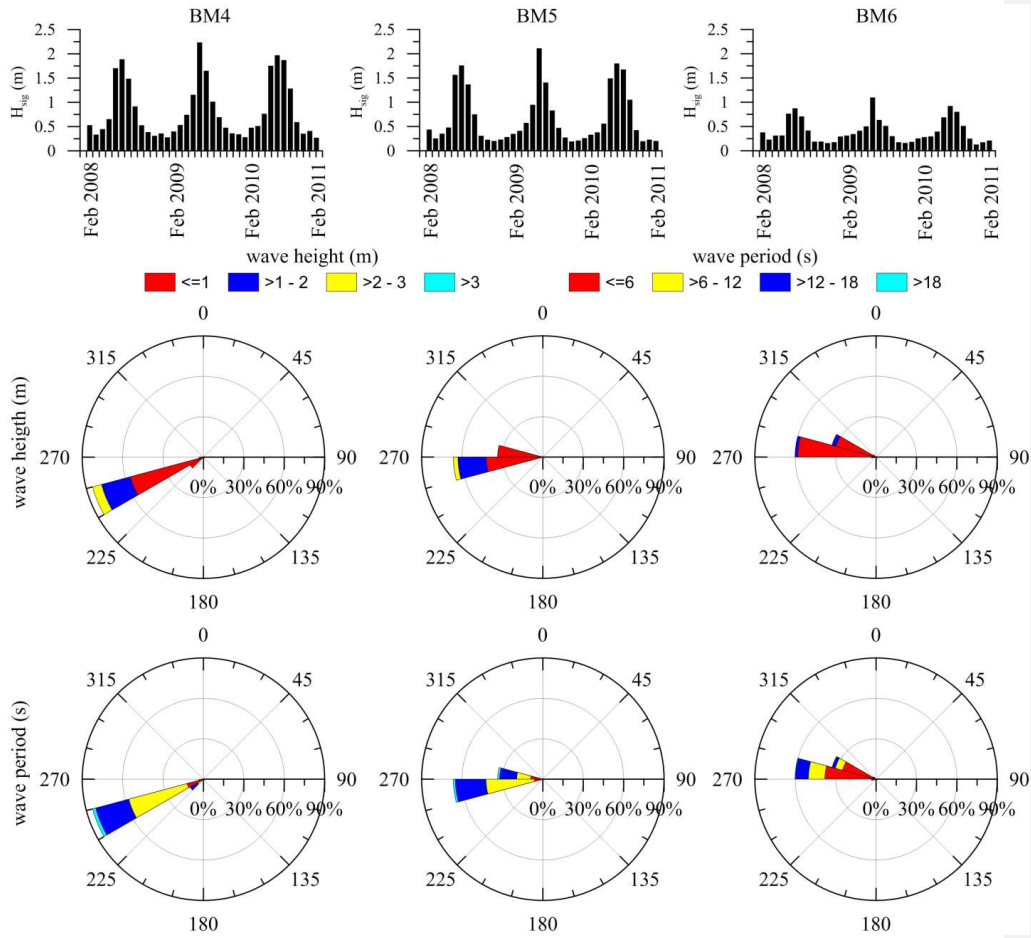


Figure5: Same as Figure 4 for locations along RT beach (BM4, BM5 and BM6).

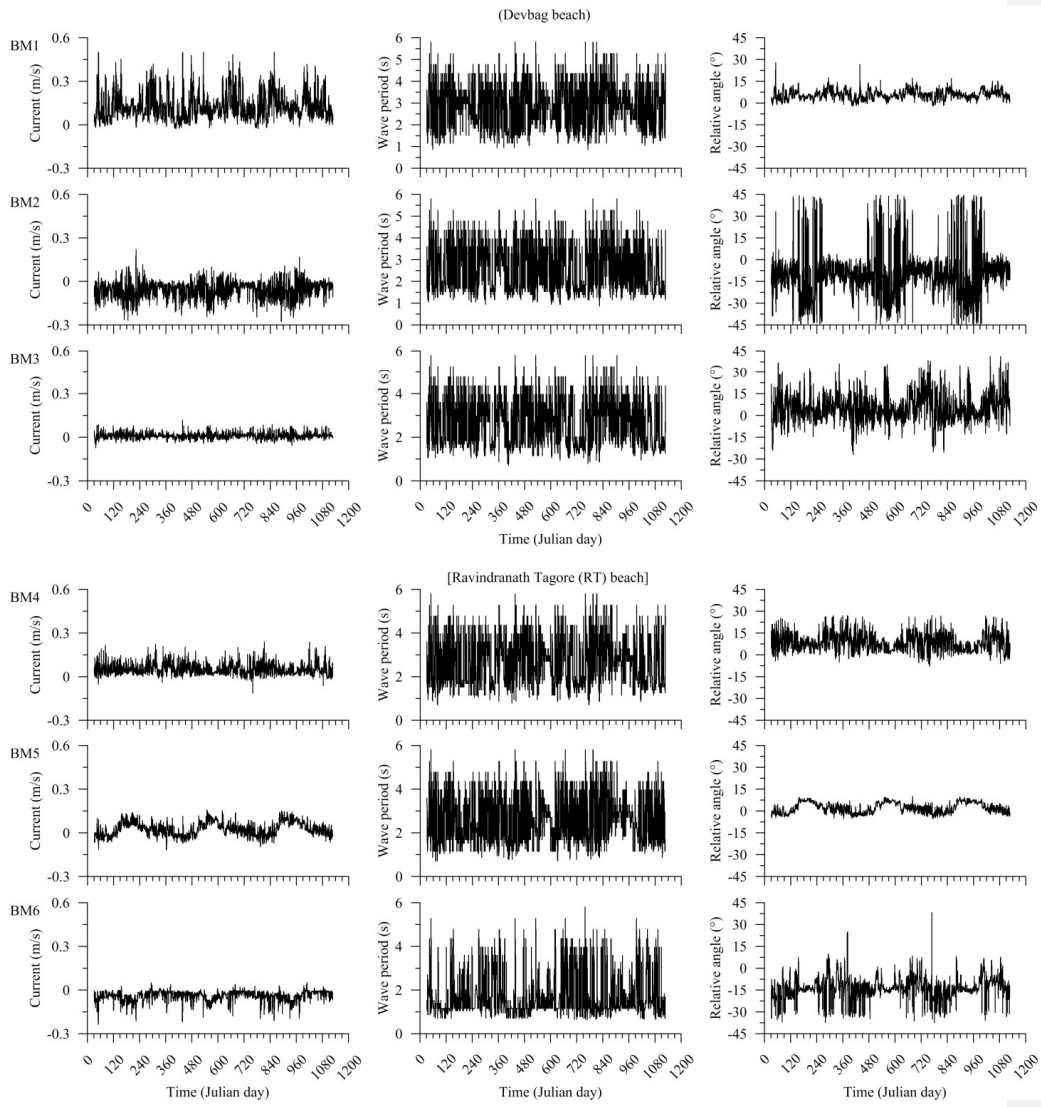


Figure6: Time series plot of mean longshore current based on Galvin approximation, wave period based on SWAN simulation, and relative angle at six locations along two beaches during February 2008 to January 2011.

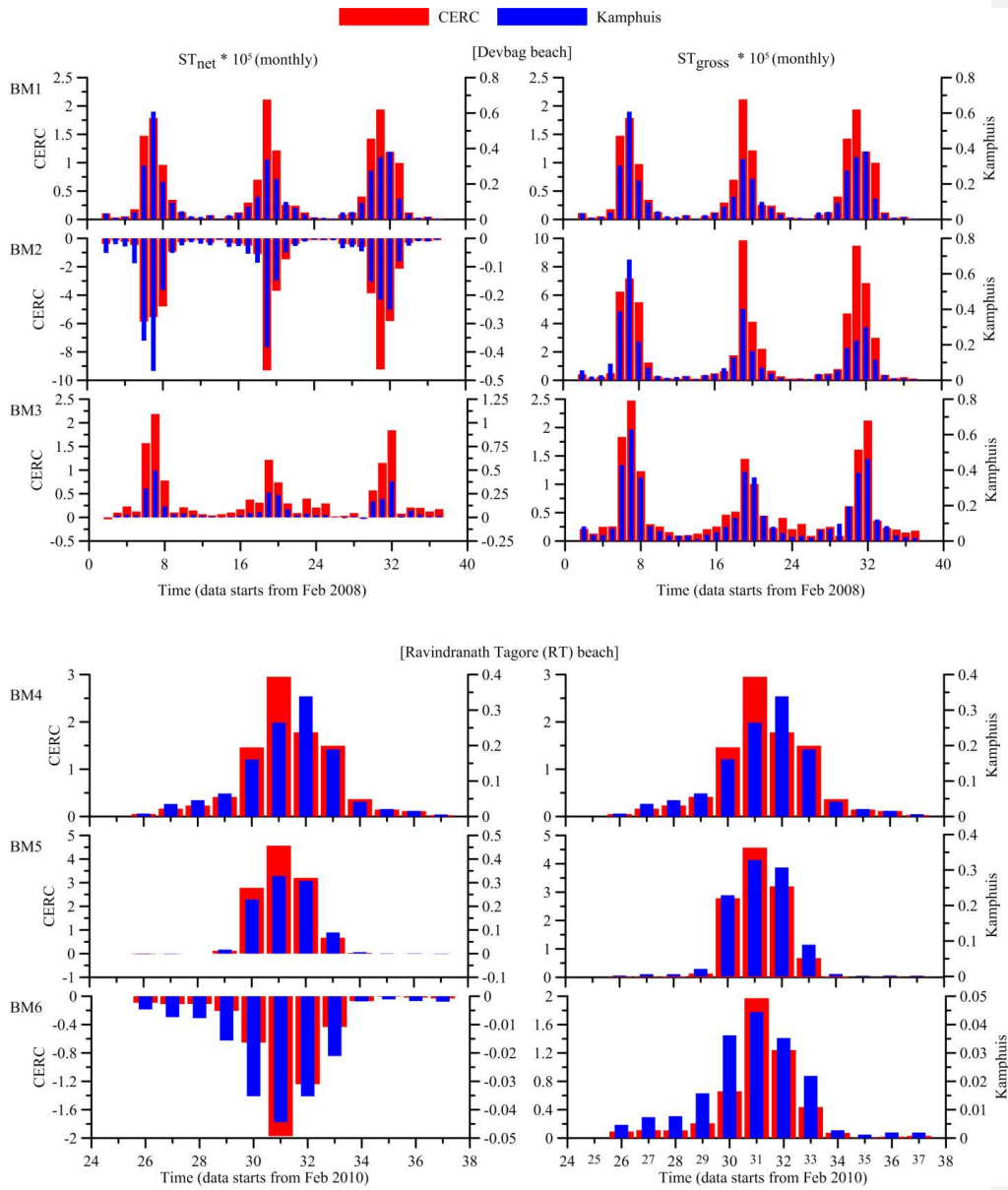


Figure 7: Monthly net (ST_{net}) and gross (ST_{gross}) sediment transport at six locations based on modified CERC and Kamphuis formulae.